Chemical Science

ROYAL SOCIETY OF CHEMISTRY

EDGE ARTICLE

View Article Online
View Journal

Cite this: DOI: 10.1039/d6sc00753h

All publication charges for this article have been paid for by the Royal Society of Chemistry

Manipulating excited-state dynamics through macrocycle positioning in a rotaxane for sensitive and discriminative methanol sensing

Yu Wang,† Yalei Ma,† Ruijuan Wen, Jing Li, Taihong Liu, Liping Ding, Rong Miao * and Yu Fang

Precise control of excited-state dynamics is essential for advancing molecular materials. Herein, we present a supramolecular strategy utilizing mechanical interlocking to regulate photophysical pathways and molecular recognition. Three rotaxanes were synthesized by positioning a dibenzo-24-crown-8 macrocycle at specific sites along a naphthalimide-based axle. Femtosecond transient absorption spectroscopy revealed that the relaxation of the excited-state is critically governed by the spatial separation: the closer the macrocycle to the fluorophore, the slower the twisted intramolecular charge transfer process. Single-crystals of the rotaxane showed a lamellar architecture, where the macrocycle acts as a pre-organized gatekeeper for the fluorophore. Therefore, highly sensitive and selective detection of methanol vapor is realized based on the rotaxane film. In addition, a portable sensor for reliable (limit of detection: 0.099% vol.), rapid (<3 s), and reusable methanol detection in adulterated beverages is achieved. Our work establishes mechanical interlocking as a versatile approach to excited-state manipulating and sensor design.

Received 27th January 2026
Accepted 4th May 2026

DOI: 10.1039/d6sc00753h

rsc.li/chemical-science

Introduction

The precise manipulation of molecular excited states is a central goal in photophysics and photochemistry, as it ultimately dictates the performance of functional materials in applications such as organic light-emitting diodes (OLEDs), solar energy conversion, and optical sensing.[1–3] Upon photoexcitation, molecules adopt unique electronic configurations that govern distinct dynamical processes, including luminescence efficiency, reactivity, and photostability.[4–6] Despite the extensive exploration of ground-state molecular libraries, the ability to predictively control excited-state dynamics remains limited.[7,8] The development of efficient strategies to direct and modulate these pathways is therefore paramount, not only for fundamental understanding but also for the rational design of advanced optical materials.

Covalent chemical synthesis has been the predominant strategy for manipulating molecular excited states. Through rational molecular design, such as introducing electron-donating/withdrawing substituents or modifying π-conjugation, key photophysical processes including twisted intramolecular charge transfer (TICT), photoinduced electron transfer (PET), and excited-state intramolecular proton transfer (ESIPT) can be effectively modulated.[9–11] Similarly, in metal complexes, altering the ligand or metal center precisely controls the nature of excited states (*e.g.*, ligand-field or metal-to-ligand charge transfer states) and spin–orbit coupling effects.[12–14] Supramolecular chemistry provides an alternative paradigm, relying on non-covalent interactions to organize chromophores and manipulate their photophysical behavior through their local environment.[15,16] This approach can promote excitonic coupling and lead to emergent excited-state species such as excimers and exciplexes.[17,18] While supramolecular strategies can circumvent intensive synthetic efforts, they often introduce new challenges: the dynamic and non-equilibrium nature of assembly processes typically results in heterogeneous populations and poorly defined excited-state structures. This inherent disorder complicates the precise manipulation and fundamental understanding of excited-state dynamics.

Mechanically interlocked molecules (MIMs), and rotaxanes in particular, offer a transformative design paradigm to address these limitations. The architecture of a rotaxane, a macrocycle threaded onto a linear axle and capped by bulky stoppers, creates a unique topology wherein the mechanical bond maintains structural integrity while enabling large-amplitude, yet controlled, translational motion of the macrocycle along the axle.[19–22] This intrinsic dynamics provides a unique platform for spatial manipulation with sub-angstrom precision, which we envisioned could be harnessed to directly regulate photophysical processes.[23,24] Specifically, the precise positioning of

Key Laboratory of Applied Surface and Colloid Chemistry, Ministry of Education, Shaanxi Provincial Key Laboratory of New Concept Sensors and Molecular Materials, School of Chemistry and Chemical Engineering, Shaanxi Normal University, Xi'an 710119, P. R. China. E-mail: miaorong2015@snnu.edu.cn

† These authors contributed equally to this work.

the macrocycle relative to an embedded fluorophore offers a novel means to manipulate excited-state dynamics through steric restriction.[25–27] Concurrently, the macrocycle can serve as a pre-organized molecular gatekeeper, sterically hindering interfering analytes from reaching the fluorophore core. Thus, the macrocycle is designed to serve a dual function: as a conformational lock to tailor photophysics and as an intrinsic molecular sieve for size-selective recognition.

In this work, we actualize this design by synthesizing a series of rotaxanes based on a naphthalimide-derived axle, with the position of a dibenzo-24-crown-8 macrocycle precisely varied along its length. We then employ femtosecond transient absorption spectroscopy combined with steady-state spectroscopy to unravel how spatial proximity governs the excited-state dynamics. Our results demonstrate that the relaxation of the excited species, particularly the TICT process, is effectively suppressed at shorter fluorophore–macrocycle distances, leading to markedly enhanced fluorescence. Meanwhile, the rotaxane exhibits a lamellar architecture in the single-crystal analysis, where the interlocked macrocycle acts as a pre-organized gatekeeper for the fluorophore. Capitalizing on these characteristics, the rotaxane-based film exhibits superior sensitivity and selectivity to methanol compared to its linear axle counterpart, facilitating the development of a portable device for the fast and reliable identification of methanol in adulterated beverages. This study thus establishes macrocycle positioning as a powerful and general strategy for manipulating molecular properties *via* mechanical bonding, opening new avenues for the creation of sophisticated functional materials.

Results and discussion

Design and synthesis of rotaxanes

The rotaxanes are composed of three parts: a donor–acceptor type fluorophore, a blocking group (bis-trifluoromethyl-substituted benzene), and a macrocycle (dibenzo-24-crown-8, D24C8). In the fluorophore, the *N*-methylindole was connected with naphthalimide through a rotatable C–C single bond, which facilitates the formation of the TICT state according to our previous work.[28,29] As shown in Fig. 1a, R-2 was synthesized using an asymmetric metal-free active templated method referring to the reported work with slight modifications.[30,31] The macrocycle in R-2 was constrained around the amide group owing to the hydrogen bonding between the N–H group and D24C8. To move the macrocycle, the N–H group was masked by *tert*-butylformate. The disruption of hydrogen bonding interactions and the considerable steric hindrance imposed by *tert*-butylformate confined the macrocycle to opposite sides of the original amide group, consequently yielding rotaxanes (R-1 and R-3) with distinct fluorophore-to-macrocycle distances.

Detailed synthesis of the compounds is shown in the SI and the identity of the rotaxanes was unambiguously determined by ^{1}H, ^{13}C NMR, and ^{19}F NMR spectroscopy as well as high-resolution mass spectrometry (Fig. S18 and S39). Fig. 1b shows partial ^{1}H NMR spectra of naked axle, R-1, R-2, and R-3 in CD_2Cl_2 at 298 K. In the spectrum of naked axle, the N–H group

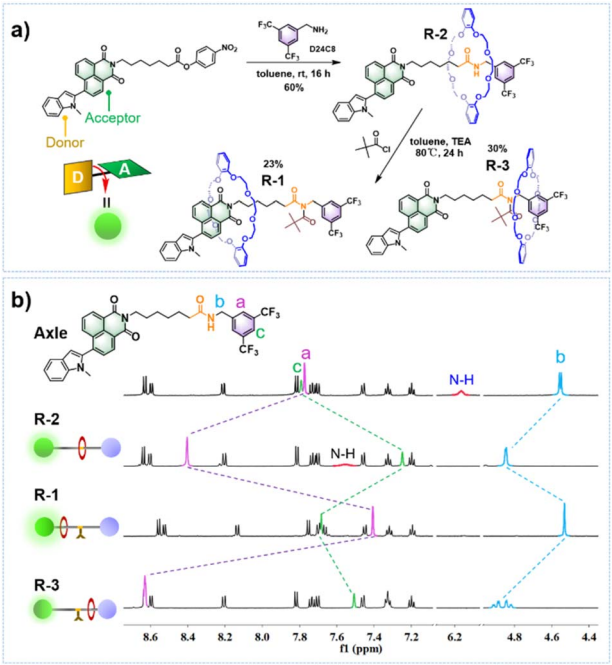

Fig. 1 (a) Synthesis route of the rotaxanes (R-1, R-2, and R-3). (b) Partial ^{1}H NMR spectra of the naked axle, R-1, R-2, and R-3 in CD_2Cl_2.

showed a single peak at ~6.1 ppm, while in the ^{1}H NMR spectrum of R-2, the peak was broadened and shifted to higher frequency (~7.6 ppm), indicating the hydrogen bonding between the N–H group and D24C8. The signal of the N–H group was absent in the ^{1}H NMR spectrum of R-1 and R-3, confirming successful masking of the N–H group. Compared to the other three compounds (R-2, R-3 and the axle), the protons on naphthalimide in R-1 showed an obvious shift upfield, indicating the interaction between naphthalimide and D24C8. Significant differences were observed in the protons on the trifluoromethyl-substituted stopper (H_a and H_c) as well as the adjacent benzyl group (H_b) in the NMR spectra. Compared to the axle, H_a and H_b in R-2 shifted to higher frequency, while H_c shifted to lower frequency. When D24C8 was shuttled to the naphthalimide (in R-1) or pushed closer to the bis-trifluoromethyl-substituted benzene stopper (R-3), the shielding effect (for H_a and H_b) and deshielding effect (for H_c) were simultaneously attenuated or enhanced, leading to systematic shifts in the corresponding peaks. Moreover, it was also obvious that the protons on the fluorophore in R-1 (8.52–8.56 ppm) shifted to higher field compared to those of R-2, R-3 and the axle (8.60–8.64 ppm). This suggests a shielding effect of the macrocycle on the fluorophore, indicating that the macrocycle approaches the fluorophore in R-1.

Photophysical properties in solution

To study photophysical properties, UV-vis and fluorescence properties of the naked axle, R-1, R-2, and R-3 in the solution state were recorded (Fig. 2 and S1–S5). UV-vis spectra of the four compounds showed features of intramolecular charge transfer (ICT) with maximum absorption around 400 nm. Spectroscopic

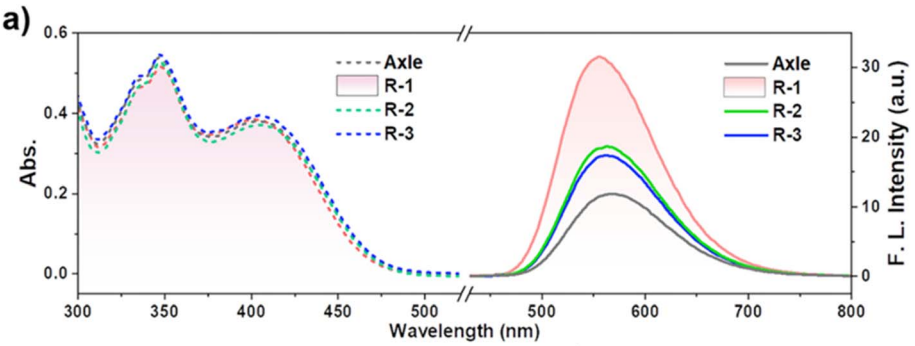

b)

Compound	λ_{abs} (nm)	λ_{em} (nm)	ε ($M^{-1}cm^{-1}$)	Stokes shift (nm)	τ (ns)
Axle	347/402	569	12103	167	2.54
R-1	347/401	555	11478	153	4.55
R-2	348/402	563	14193	161	3.44
R-3	345/405	563	15590	159	3.23

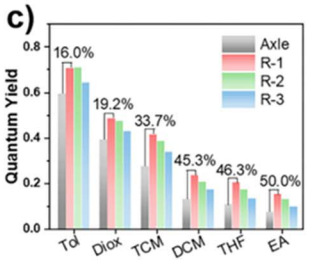

Fig. 2 Photophysical properties of the axle, R-1, R-2, and R-3 in the solution state. (a) UV-vis and fluorescence spectra of the four compounds in dichloromethane. (b) Summarized photophysical properties of the four compounds. (c) Absolute fluorescence quantum yield of the four compounds in different solvents (Tol: toluene; Diox: 1, 4-dioxane; TCM: trichloromethane; DCM: dichloromethane; THF: tetrahydrofuran; EA: ethyl acetate). Compound concentration: 5.00×10^{-6} M. The values above the bars indicate the relative enhancement in quantum yield for R-1 compared to axle, calculated as $\frac{\varphi_{R_1} - \varphi_{axle}}{\varphi_{axle}} \times 100\%$.

studies revealed that the key distinctions between the molecular axle and the rotaxanes lie in their fluorescence characteristics (Fig. 2a). The rotaxanes exhibited a hypsochromic effect as well as enhanced fluorescence intensity in fluorescence spectra compared to that of the axle. Notably, R-1 showed a hypsochromic shift of 14 nm in the maximum emission and more than twice the fluorescence intensity of the axle at the same molar concentration. Furthermore, a clear trend is evident across the series from R-1 to R-3. Both the fluorescence lifetime (Fig. 2b) and quantum yield (Fig. 2c) follow the order R-1 > R-2 > R-3. As solvent polarity increased, fluorescence quantum yields of all the four compounds dramatically decreased, due to the facilitated formation of the TICT state in highly polar solvents.[32] Fluorescence of the compounds was nearly quenched in protonic solvents, like methanol and ethanol (Fig. S5). It was also noticed that the proportion of the fluorescence quantum yield of the rotaxanes to that of the free axle significantly increased (from 16% to 50%) upon increasing the solvent polarity from toluene to ethyl acetate.

To further investigate the effect of mechanical bonding on fluorescence emission, fluorescence responses of the compounds to viscosity and temperature were studied. TICT fluorophores are usually sensitive to viscosity, as the intramolecular twisting would be restricted in viscous system, leading to fluorescence enhancement.[33,34] Fig. 3a shows fluorescence spectra of the four compounds in solutions with different methanol/glycerol ratios.

At the initial stage, the fluorescence intensity changed only marginally with the increasing proportion of glycerol. However, a significant enhancement in fluorescence intensity was observed in the rotaxanes when the glycerol proportion reached 90%. The enhancement for the three rotaxanes followed the order of R-1 (64 times) > R-2 (40 times) > R-3 (15 times), which may be in the reverse order of the tendency of intramolecular rotation. No significant enhancement was observed in the emission spectra of the axle, indicating higher intramolecular rotation tendency in the axle than that in the rotaxanes.

Considering the significant influence of temperature on the mechanical bond as well as molecular conformations,[35,36] fluorescence spectra of the axle and the rotaxanes at varied temperatures were recorded. All four compounds exhibited negative thermal quenching as evidenced by the enhanced emission upon increasing temperature (Fig. 3b–c and S6–S7). This can be attributed to an increased population of the locally excited (LE) state and a diminished contribution from the twisted intramolecular charge transfer (TICT) state, a trend which has also been reported in other naphthalimide derivatives.[37,38] The plots of fluorescence intensity *versus* temperature for the rotaxanes exhibited steeper slopes than those for the axle, indicating a more effective suppression of the TICT state with increasing temperature in rotaxanes. When the temperature increased from 10 °C to 60 °C, the fluorescence intensity of R-2 showed a twofold increase over that observed for the free axle.

The results from both viscosity and temperature studies verified the conspicuous effect of mechanical bonding on fluorescence emission and implied its influence on the excited-state dynamics. To gain deeper insights into the excited-state dynamics, transient absorption spectroscopy was employed.

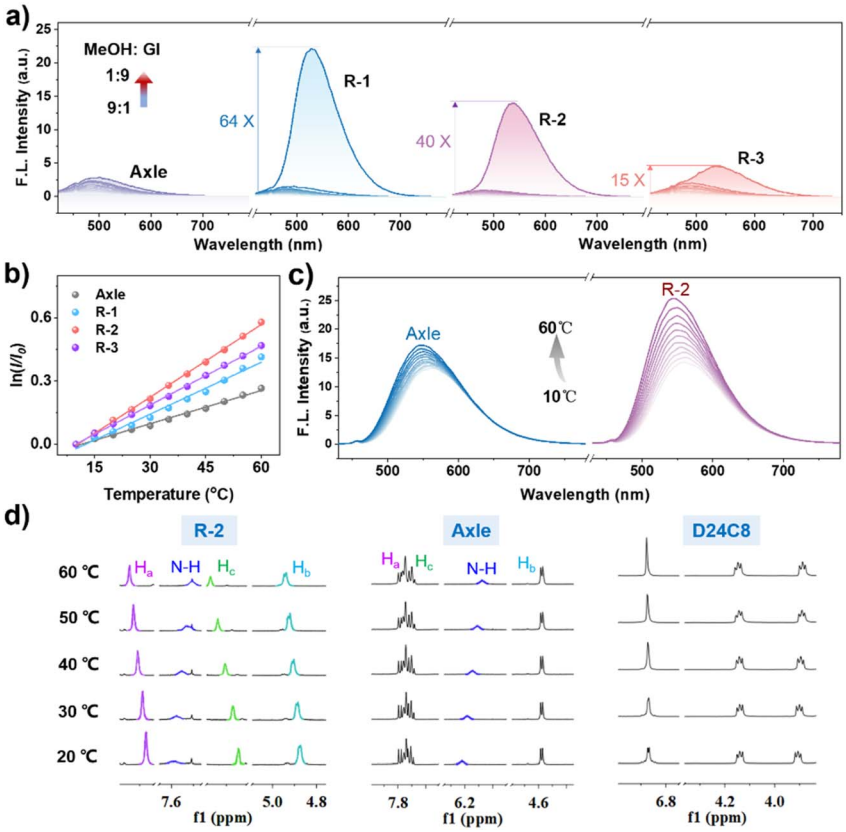

Fig. 3 (a) Fluorescence spectra of the axle, R-1, R-2, and R-3 in methanol/glycerol mixtures with varied ratios. (b) Plots of fluorescence intensity of the axle, R-1, R-2, and R-3 *versus* temperature. Solvent: THF. (c) Fluorescence spectra of the axle and R-2 in THF at different temperatures (10–60 °C). (d) Partial ^{1}H NMR spectra of R-2, the axle and D24C8 in $CDCl_3$. Compound concentration for (a–c): 5.00×10^{-6} M.

To understand the influence of temperature on mechanical binding, temperature-dependent ^{1}H NMR spectra of R-2, the axle and D24C8 were recorded (Fig. 3d and S8–S10). Negligible shifts were observed for the protons on D24C8. It was found that the N–H signal in both R-2 and the axle shifted to lower frequency with increasing temperature, which reflects hydrogen bonding between N–H and the solvent. While the three protons (H_a, H_b and H_c) participating in the formation of the mechanical bond in R-2 shifted to higher frequency, this could be hardly observed in the axle. With these results, it is reasonable to deduce that the mechanical bond is sensitive to temperature, which leads to the remarkable fluorescence enhancement in the rotaxanes upon increasing temperature.

Fs-TA experiments of the free axle, R-1, R-2 and R-3 in tetrahydrofuran were conducted, and the global analysis was performed to reveal the relaxation mechanism (Fig. 4 and S11–S14). All the four compounds showed similar spectral evolution scenarios (Fig. S11), where the excited species underwent transitions from the LE state to the ICT state, and subsequently to the TICT state. Fs-TA pseudo-color maps and representative kinetics of the excited species (LE, ICT and TICT) of the axle and R-1 are shown in Fig. 4a and b. It is clear that R-1 exhibited a smaller population of the TICT state and a delayed onset of its formation compared to the naked axle. According to transient spectroscopy, the lifetimes of the excited species (LE, ICT, and TICT) in the four compounds (axle, R-1, R-2, and R-3) were calculated (Fig. S14). A slight difference was found in the lifetime of the LE state; however, the lifetimes of both ICT and TICT states of the rotaxanes were significantly longer than that of the axle. k_{TICT} (Fig. 4c) of the four compounds followed the order axle > R-1 > R-2 > R-3, which is opposite to that of the fluorescence intensity (*e.f.* Fig. 2). These results confirm the distance-dependence of the TICT state on the macrocycle–fluorophore separation.

As inferred from stationary and transient spectroscopy, the excited-state relaxation mechanism of the rotaxanes is summarized in Fig. 4c. It is demonstrated that the TICT kinetics can be effectively regulated through precise control of the macrocycle's position, thereby establishing the mechanical bond as a powerful tool for manipulating excited-state dynamics and paving the way for future innovative work in molecular photophysics.

Molecular packing in single crystals and methanol sensing

To further consolidate the molecular structure and study the intermolecular interactions between the rotaxane molecules, single crystals were prepared through solvent evaporation. As shown in Fig. 5a, the single crystal of R-2 is monoclinic and is characterized by a lamellar structure, where the naphthalimide moieties and the bonded macrocycles are stacked in an

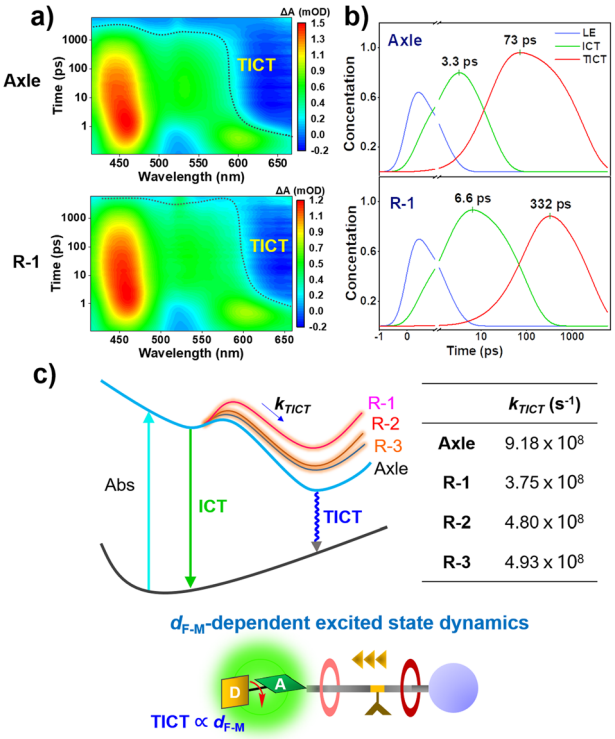

Fig. 4 (a) The fs-TA pseudo-color maps of the naked axle and R-1 in THF. Compound concentration: 5.0×10^{-5} M. (b) The distribution of excited-state species (LE, ICT and TICT) in the naked axle and R-1 as a function of time. (c) Schematic illustration of excited-state relaxation pathways of the four compounds (axle, R-1, R-2, and R-3), the formation rate constant of the TICT state, and the illustration of the supramolecular strategy for excited-state dynamics manipulation, referring to the Marcus theory, $k \propto \exp\left(-\frac{(\lambda+\Delta G)^2}{4\lambda k_B T}\right)$, where ΔG represents the change in reaction free energy.

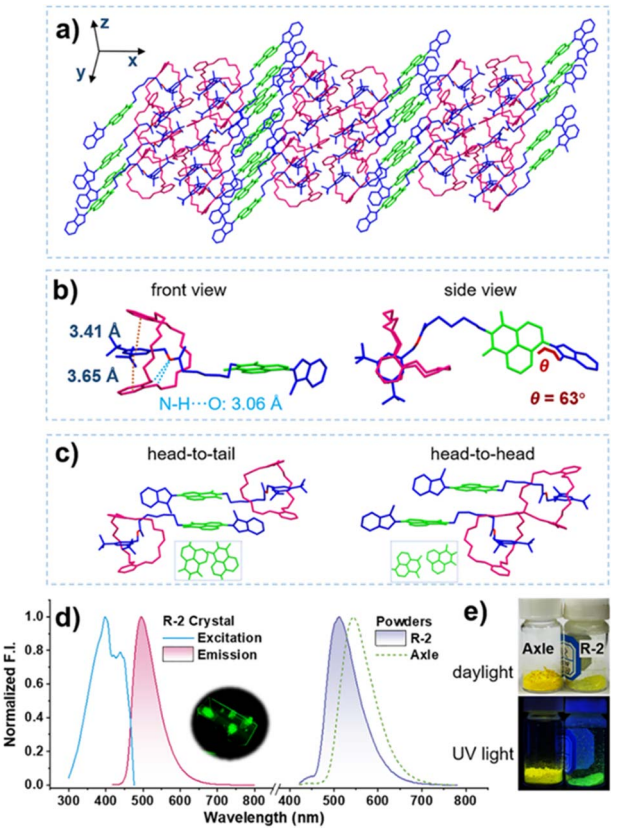

Fig. 5 Molecular packing (a), molecular structure (b), and two types of dimers (c) in the single crystal of R-2. (d) Normalized fluorescence emission/excitation spectra of R-2 crystals, R-2 powder, and the axle powder. (e) Images of powders of the naked axle and R-2 under daylight and 365 nm UV light.

alternating fashion. The structure of a single R-2 molecule in the crystal is illustrated in Fig. 5b. As expected, the macrocycle is located around the amide group owing to significant hydrogen bonding between the N–H group and D24C8 (~3.06 Å), which is consistent with the discussion in the NMR study (*e.f.* Fig. 1).

The front view revealed that D24C8 adopted a boat-like conformation, in which the flexible crown ether chain formed the hull, while the two phenyl rings were bent upward.

Interestingly, a π-stacked sandwich configuration was observed between the two phenyl rings of D24C8 and the bis(trifluoromethyl)benzene ring, with interplanar distances of 3.41 Å and 3.65 Å, respectively. Additionally, a nearly perfect overlap of these three phenyl rings was found in the side view, indicating sufficient π–π interactions within the molecule.[39,40] Further inspection of the intermolecular interactions within the single crystal revealed that two R-2 molecules were arranged in either a head-to-head or head-to-tail fashion (Fig. 5c). van der Waals forces were identified as the dominant interaction, as close π–π stacking between the naphthalimide rings was precluded by the pronounced steric hindrance from both sides. This is favorable for solid-state fluorescence, as close π–π stacking may cause excitonic coupling and lead to fluorescence quenching.

Fig. 5d shows the normalized fluorescence spectra of R-2 and the naked axle in the solid state. Although R-2 and the naked axle showed almost the same emission wavelength in solution (*e.f.* Fig. 2), they exhibited different fluorescence behaviors in the solid state. While the powder of the axle was bright yellow with a maximum emission wavelength (λ_{max}) of ~545 nm, both the powder and crystal of R-2 emitted bright green fluorescence ($\lambda_{max} \approx$ 512 nm and 495 nm). This result is reasonable as π–π interaction between the adjacent naphthalimide rings was hardly observed in the crystal. Meanwhile, the pronounced hypsochromic shift in the fluorescence spectra of the rotaxane in solid states, compared to the naked axle, demonstrates the critical role of the macrocycle in intermolecular stacking. The abundant macrocycle rings would also create a unique microenvironment for the fluorophores, which may establish a foundation for selective molecular sensing.

Methanol is highly toxic to humans and can cause severe illness or even death.[41,42] Traces of methanol are naturally present in some beverages, such as commercially produced wine and beer, which are safe to consume. However, it can be deadly in large quantities, and illegal breweries sometimes use methanol as a cheap substitute for ethanol. It is difficult to

detect the presence of methanol in contaminated beverages, as it looks, smells, and tastes like regular ones. A portable and easy-to-operate sensor for reliable methanol detection would provide consumers with robust food safety assurance. While facile and efficient strategies such as chemo-resistive gas sensors combined with separation columns,[43,44] nanofilms constructed using designed building blocks,[45] and push–pull fluorophores have been explored in recent years,[46,47] they often suffer from drawbacks including dependent on high-performance separation materials, synthetic complexity, or slow response kinetics. Nevertheless, sensors that can directly and selectively detect methanol over ethanol are urgently needed.

Based on the results from fluorescence studies, we hypothesized that fluorescence of the rotaxane in the solid state could be quenched upon exposure to methanol vapors. Concurrently, the surrounding D24C8 was expected to provide a molecular sieving effect, facilitating differentiation of methanol from ethanol and other species. This synergistic effect would enable highly selective and efficient methanol sensing without the need of sample pretreatment.

To verify the hypothesis, we prepared fluorescent films by drop-casting the solutions of R-2 or the naked axle onto a glass sheet (1.2 × 1.2 cm), which were subsequently assembled into a portable device (3 × 4 × 4 cm^3; Fig. 6a). Fluorescence responses of the film-based devices to methanol and other interferences are shown in Fig. 6b. It was found that the film of R-2 (Film-R) exhibited a remarkable fluorescence quenching efficiency of >50% for methanol vapor, which is more than four times that of the axle film (Film-A), suggesting preferrable sensitivity of Film-R. The response of Film-R to ethanol was less than one-fourth of that to methanol, while the response of Film-A to ethanol was more than one-third of that to methanol, indicating higher selectivity of Film-R for methanol over ethanol than Film-A. Therefore, methanol can be easily differentiated even in a high (>90%) background of ethanol in methanol/ethanol mixtures (Fig. S15). It was also noted that Film-R (1/6) demonstrated superior resistance to acetone during methanol sensing compared to Film-A (1/3). All other recognized interferences in methanol detection, such as water, tetrahydrofuran, *n*-hexane, and toluene caused negligible fluorescence responses, suggesting excellent selectivity of the sensor. In addition, the fluorescence response of the films of R-1 and R-3 was also investigated (Fig. S16). Similar to R-2, R-1 and R-3 also exhibited doubled fluorescence quenching efficiency in methanol sensing compared to the axle, inferring the advantages of the as-synthesized rotaxanes in methanol sensing.

Sensitivity of the Film-R-based sensor was investigated by recording responses of the sensor to air/methanol mixtures with varied methanol contents (Fig. 6c). A distinguishable response was noticed when a low methanol concentration of 0.12% vol. was pumped into the system. With the increase in methanol concentration, the responses gradually intensified. A good linear relationship ($R^2 = 0.99$) between response intensity and the concentration of methanol vapor was obtained. The limit of detection was calculated to be 0.099% vol. using the signal-to-noise approach (SI). Furthermore, the device exhibited a fast response (<3 s) and outstanding reversibility, with little signal degradation over 40 consecutive cycles (Fig. 6d).

Leveraging its superior sensitivity and selectivity, as well as reusability, the Film-R-based methanol senor was utilized for detecting illegal methanol adulteration in alcoholic beverages (Fig. 6e). Different amounts of methanol (2–20% vol.) were added to the beverages obtained from trusted sources and the mixtures were sealed and left for 24 h under ambient condition (25 °C) to reach vapor–liquid equilibrium. The equilibrated vapor phase was then pumped into the sensor for the assessment of adulteration. Responses of the senor to liquor and beer

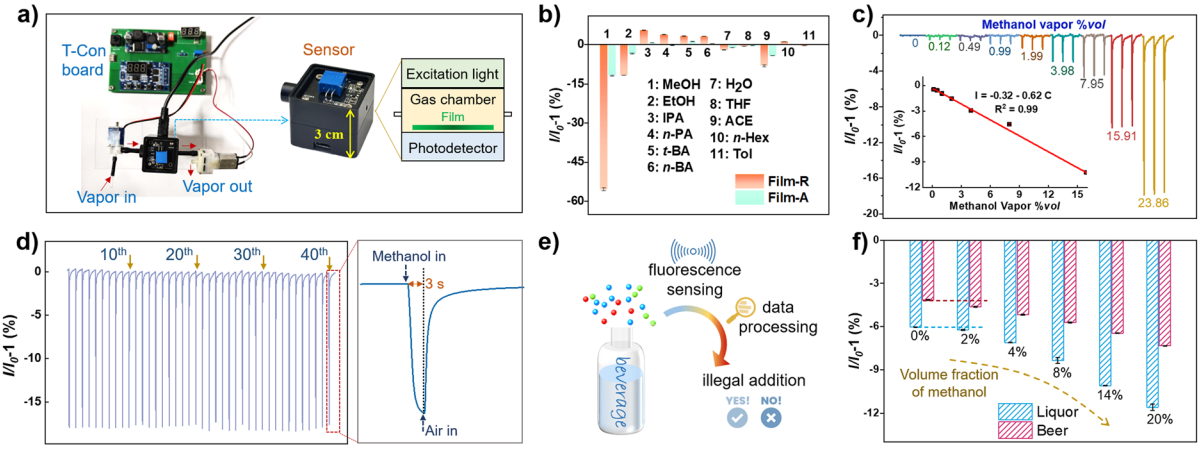

Fig. 6 (a) Photograph of the homemade sensing platform and the detailed layout of the portable sensor device. (b) Fluorescence responses of Film-R and Film-A to different types of volatile organic compounds and water. MeOH: methanol; EtOH: ethanol; IPA: isopropyl alcohol; *n*-PA: *n*-propanol; *t*-BA: *tert*-butyl alcohol; *n*-BA: *n*-butanol; THF: tetrahydrofuran; ACE: acetone; *n*-Hex: *n*-hexane; Tol: toluene. (c) Responses of the Film-R sensor to vapors with varied methanol concentrations (0.12–23.86% vol.). The inset plots show the linear relationship between response intensity and methanol concentration. (d) Forty reversible sensing cycles of the Film-R sensor to methanol vapor (23.86% vol.). (e) Schematic illustration of the identification of illegal methanol addition using the Film-R sensor. (f) Responses of the Film-R sensor to liquor (blue) and beer (red) with different amounts of methanol added.

adulterated with varying methanol concentrations are presented by the blue and red data series (Fig. 6f), respectively. As shown in the figure, both systems exhibited a consistent trend: the signal response progressively intensifies with increasing methanol content (Fig. S17). Accordingly, detection limits for methanol in liquor and beer were calculated to be 0.10% vol. and 0.19% vol., respectively, offering a powerful tool for identifying adulterated as well as low-quality alcoholic beverages.

The outstanding performance of the portable methanol sensor, demonstrated in the detection of adulterated beverages, showcases the great potential of Film-R for real-world applications. Furthermore, this work highlights the critical role of mechanical interlocking in regulating excited states and developing smart materials.

Conclusions

In this work, we have achieved precise manipulation of excited-state dynamics through a mechanical interlocking strategy in a series of rationally designed rotaxanes. These rotaxanes consist of a molecular axle bearing a fluorophore, threaded by a crown ether (D24C8) that is strategically confined at specific positions along the fluorophore. The photophysical properties of the fluorophore are highly dependent on the fluorophore–macrocycle distance, where close spatial proximity of D24C8 leads to a marked increase in the fluorescence quantum yield. Femtosecond transient absorption spectroscopy further reveals a distinct divergence in the excited-state species distribution between the rotaxane and its molecular axle. Notably, the population of the TICT state is significantly suppressed in the rotaxane relative to the free axle, a consequence of restricted molecular motion imposed by mechanical interlocking. Beyond influencing excited-state dynamics, D24C8 also provides a unique microenvironment for the fluorophore, as evidenced by the observed lamellar structure in the single crystal. Leveraging these properties, we realized sensitive and selective methanol detection over ethanol and other analogues using a rotaxane-based film, which was subsequently integrated into a portable device for rapid and reliable identification of methanol-adulterated beverages. Overall, this work underscores the potential of mechanical interlocking not only for manipulating excited-state dynamics but also for enabling advanced molecular sensing.

Author contributions

R. M. conceived the study. Y. W. and Y. M. conducted the experiments. All authors contributed to writing and revising the manuscript.

Conflicts of interest

There are no conflicts to declare.

Data availability

CCDC 2500809 (for R-2) contains the supplementary crystallographic data for this paper.[48]

The data supporting this article have been included as part of the supplementary information (SI). Supplementary information: SI figures, NMR spectra, and further experimental details. See DOI: https://doi.org/10.1039/d6sc00753h.

Acknowledgements

The authors acknowledge funding from the National Key Research and Development Program of China (2022YFA1205502), the National Natural Science Foundation of China (22072084 and 22132002), and the Ministry of Education of the People's Republic of China (B14041, 111 Project).

Notes and references

1 A. Cotic, S. Cerfontaine, L. D. Slep, B. Elias, L. Troian-Gautier and A. Cadranel, *J. Am. Chem. Soc.*, 2023, **145**, 5163–5173.
2 K. Liu, J. Zhang, Q. Shi, L. Ding, T. Liu and Y. Fang, *J. Am. Chem. Soc.*, 2023, **145**, 7408–7415.
3 X. Wu, S. Ni, C.-H. Wang, W. Zhu and P.-T. Chou, *Chem. Rev.*, 2025, **125**, 6685–6752.
4 L. Cui, Y. Gong, C. Cheng, Y. Guo, W. Xiong, H. Ji, L. Jiang, J. Zhao and Y. Che, *Adv. Sci.*, 2021, **8**, 2002615.
5 R. Kimura, H. Kuramochi, P. P. Liu, T. Yamakado, A. Osuka, T. Tahara and S. Saito, *Angew. Chem., Int. Ed.*, 2020, **59**, 16430–16435.
6 S. Lin, X. Wang, H. Li, J. Zhou, R. Wen, J. Ma, S. Yin, L.-Y. Peng, H. Peng and Y. Fang, *Nat. Commun.*, 2025, **16**, 8130.
7 Z. Y. Liu, Q. B. Nie, B. L. Han, R. K. Gupta, G. L. Dong, G. G. Luo, Z. L. Yang and D. Sun, *Chem. Soc. Rev.*, 2025, **54**, 9092–9115.
8 V. W.-W. Yam, *Nat. Synth.*, 2023, **2**, 94–100.
9 Z. Han, M. He, G. Wang, J. M. Lehn and Q. Li, *Angew. Chem., Int. Ed.*, 2024, **63**, e202416363.
10 K. Hanaoka, S. Iwaki, K. Yagi, T. Myochin, T. Ikeno, H. Ohno, E. Sasaki, T. Komatsu, T. Ueno, M. Uchigashima, T. Mikuni, K. Tainaka, S. Tahara, S. Takeuchi, T. Tahara, M. Uchiyama, T. Nagano and Y. Urano, *J. Am. Chem. Soc.*, 2022, **144**, 19778–19790.
11 L. Zeng, L. Huang, Z. Huang, T. Mani, K. Huang, C. Duan and G. Han, *Nat. Commun.*, 2024, **15**, 7270.
12 J. Niu, F. Gao, Y. Wang, W. Lu, J. Zhang, J. He, X. Lou, Y. Ma, C. Duan, C. Han and H. Xu, *Angew. Chem., Int. Ed.*, 2025, **64**, e202508667.
13 W. Wang and L. Liu, *Dyes Pigm.*, 2022, **200**, 110112.
14 K. Xu, J. Zheng, F. Zhan, W. Lou, X. Fang, Q. Chen, H. Guo, W. Chen, Y.-F. Yang, Y. She and G. Li, *Chem. Eng. J.*, 2025, **506**, 159948.
15 N. Bäumer, S. Yamada, S. Ogi and S. Yamaguchi, *J. Am. Chem. Soc.*, 2025, **147**, 8300–8311.

16 S. Garain, S. M. Wagalgave, A. A. Kongasseri, B. C. Garain, S. N. Ansari, G. Sardar, D. Kabra, S. K. Pati and S. J. George, *J. Am. Chem. Soc.*, 2022, **144**, 10854–10861.
17 J. L. Han, S. Fujikawa and N. Kimizuka, *Angew. Chem., Int. Ed.*, 2024, **63**, e202410431.
18 C. Kaufmann, W. Kim, A. Nowak-Król, Y. Hong, D. Kim and F. Würthner, *J. Am. Chem. Soc.*, 2018, **140**, 4253–4258.
19 E. Moulin, L. Faour, C. C. Carmona-Vargas and N. Giuseppone, *Adv. Mater.*, 2020, **32**, 1906036.
20 J. P. Sauvage, *Angew. Chem., Int. Ed.*, 2017, **56**, 11080–11093.
21 M. Xue, Y. Yang, X. Chi, X. Yan and F. Huang, *Chem. Rev.*, 2015, **115**, 7398–7501.
22 L. M. Zhao, L. S. Zheng, X. P. Wang and W. Jiang, *Angew. Chem., Int. Ed.*, 2022, **61**, e202214296.
23 E. M. Pérez, D. T. F. Dryden, D. A. Leigh, G. Teobaldi and F. Zerbetto, *J. Am. Chem. Soc.*, 2004, **126**, 12210–12211.
24 Q. C. Wang, D. H. Qu, J. Ren, K. C. Chen and H. Tian, *Angew. Chem., Int. Ed.*, 2004, **43**, 2661–2665.
25 J. Y. Lau, C. C. Shaffer, H. S. Sanders and B. D. Smith, *J. Phys. Chem. A*, 2025, **129**, 11281–11293.
26 M. Dharmarwardana, J. M. Dempsey, S. Padilla-Coley, T. S. Jarvis, K. Shi, K. M. Atkinson and B. D. Smith, *Chem. Commun.*, 2021, **57**, 13518–13521.
27 H. V. Schröder, S. Sobottka, M. Nößler, H. Hupatz, M. Gaedke, B. Sarkar and C. A. Schalley, *Chem. Sci.*, 2017, **8**, 6300–6306.
28 R. Miao, J. Li, C. Wang, X. Jiang, Y. Gao, X. Liu, D. Wang, X. Li, X. Liu and Y. Fang, *Adv. Sci.*, 2022, **9**, 2104609.
29 W. Zhang, J. Kong, R. Miao, H. Song, Y. Ma, M. Zhou and Y. Fang, *Adv. Funct. Mater.*, 2024, **34**, 2311404.
30 C. Tian, S. D. P. Fielden, B. Pérez-Saavedra, I. J. Vitorica-Yrezabal and D. A. Leigh, *J. Am. Chem. Soc.*, 2020, **142**, 9803–9808.
31 C. Tian, S. D. P. Fielden, G. F. S. Whitehead, I. J. Vitorica-Yrezabal and D. A. Leigh, *Nat. Commun.*, 2020, **11**, 744.
32 S. Wiedbrauk, B. Maerz, E. Samoylova, A. Reiner, F. Trommer, P. Mayer, W. Zinth and H. Dube, *J. Am. Chem. Soc.*, 2016, **138**, 12219–12227.
33 Y. Ma, Q. Wang, J. Deng, X. Yan, J. Liu, L. Ding, R. Miao and Y. Fang, *Macromol. Rapid Commun.*, 2024, **45**, 2300592.
34 Y. Zhou, Q. Wang, S. Chanmungkalakul, X. Wu, H. Xiao, R. Miao, X. Liu and Y. Fang, *Chem. Eur. J*, 2024, **30**, e202303707.
35 A. Matsumoto, K. Nakagawa, T. Nakanishi, A. Sekine, S. Kojo, M. Kira, S. Sato, N. Shibata and T. Asahi, *J. Am. Chem. Soc.*, 2025, **147**, 11988–11997.
36 K. Zhu, G. Baggi and S. J. Loeb, *Nat. Chem.*, 2018, **10**, 625–630.
37 J. Feng, K. J. Tian, D. H. Hu, S. Q. Wang, S. Y. Li, Y. Zeng, Y. Li and G. Q. Yang, *Angew. Chem., Int. Ed.*, 2011, **50**, 8072–8076.
38 Y. Yu, N. Qiang, Z. Liu, M. Lu, Y. Shen, J. Zou, J. Yang and G. Liu, *Nanomaterials*, 2024, **14**, 1255.
39 J. Dai, S. Qi, M. Zhao, J. Liu, T. Jia, G. Liu, F. Liu, P. Sun, B. Li, C. Wang, J. Zhou and G. Lu, *Chem. Eng. J.*, 2023, **471**, 144745.
40 C. Wang, W. Chi, Q. Qiao, D. Tan, Z. Xu and X. Liu, *Chem. Soc. Rev.*, 2021, **50**, 12656–12678.
41 S. Cousins, *Lancet*, 2025, **406**, 1326–1327.
42 J. Zheng, T. Zhang, H. Zeng, W. Guo, B. Zhao, Y. Sun, Y. Li and L. Jiang, *Small*, 2019, **15**, 1804688.
43 J. van den Broek, S. Abegg, S. E. Pratsinis and A. T. Güntner, *Nat. Commun.*, 2019, **10**, 4220.
44 Z. Wang, M. Bu, N. Hu and L. Zhao, *Compos. Part. B. Eng.*, 2023, **248**, 110378.
45 J. Shin, K. Kim, I. S. Min, M. Sang, J. Y. Lee, K. Hwang, Y. Kang, J. Kim and K. J. Yu, *Adv. Funct. Mater.*, 2025, **35**, 2419110.
46 Q. Liu, Q. Sun, J. Shen, H. Li, Y. Zhang, W. Chen, S. Yu, X. Li and Y. Chen, *Coord. Chem. Rev.*, 2023, **482**, 215078.
47 K. Wang, C. Bi, L. Zelenkov, X. Liu, M. Song, W. Wang, S. Makarov and W. Yin, *ACS Sens.*, 2024, **9**, 5708–5727.
48 CCDC 2500809: Experimental Crystal Structure Determination, 2026, DOI: 10.5517/ccdc.csd.cc2py987.